Infrared dynamics of $YbIn_{1-x}Ag_xCu_4$: Kondo scaling, sum rules, and temperature dependence

Jason N. Hancock,*,† Tim McKnew, and Zack Schlesinger
Physics Department, University of California Santa Cruz, Santa Cruz, California 95064, USA

John L. Sarrao
Los Alamos National Laboratory, Mail Stop K764, Los Alamos, New Mexico 87545, USA

Zach Fisk
National High Magnetic Field Laboratory, Tallahassee, Florida 32310, USA
and Department of Physics, University of California Davis, Davis, California 95616, USA
(Received 28 October 2004; revised manuscript received 5 December 2005; published 28 March 2006)

We present an infrared/optical study of the dynamics of the strongly correlated electron system $YbIn_{1-x}Ag_xCu_4$ as a function of composition and temperature for x ranging from 0 to 1, and T between 20 and 300 K. $YbIn_{1-x}Ag_xCu_4$ evolves from a mixed-valent system at low x to a heavy-Fermion system at high x, and exhibits an unusual electronic phase transition in the low x region. This paper reveals information about the unusual phase transition as well as the phases themselves. Scaling relations emerge from the data and are investigated in detail using a periodic Anderson model based calculation. We also explore the temperature dependence of $\sigma_1(\omega)$ and the infrared sum rule behavior, and provide a picture in which to view both the low- and high-energy x-dependent features of the infrared data.

DOI: 10.1103/PhysRevB.73.125119 PACS number(s): 71.27.+a, 75.20.Hr, 75.30.Mb

When exploring the complex terrain of correlated electron phases, one is often interested in the phase boundaries separating systems which are controlled by different physics. In the low doping regime ($x<0.2$) of $YbIn_{1-x}Ag_xCu_4$, a temperature-driven, first-order electronic phase transition separates two phases which are characterized by widely disparate effective energy scales (T_K) associated with the effects of hybridization between the localized Yb f electrons and the itinerant conduction electrons. This rapid change provides both an opportunity to identify and isolate features associated with many-body hybridization physics and raises fundamental questions regarding the origin of the transition itself.

The valence transition in $YbInCu_4$ has been examined with a variety of experimental techniques,[1–7] and exhibits some similarities[8–10] to phase transitions observed in certain rare earth intermetallic compounds.[11,12] Samples of high quality can be made, and provide the only known example of a valence transition occurring at ambient pressure in a stoichiometric sample. The synthesis of high quality single crystal samples has allowed the detailed study of the phase diagram of $YbIn_{1-x}Ag_xCu_4$, and continued effort has revealed a tendency of the system to order ferromagnetically as the phase transition temperature is driven to zero either by pressure[13,14] or Y doping.[13,15] The presence of interesting phase competition in a system where the sample chemistry is well controlled enhances our interest in this correlated electron system.

Figure 1 shows a schematic representation of the phase diagram of $YbIn_{1-x}Ag_xCu_4$. At low doping, a line of first order phase transitions separates a low temperature, mixed-valent phase and a high temperature local moment phase. In $YbInCu_4$ ($x=0$) at high temperature ($T>T_v=42$ K), the magnetic response exhibits a Curie-Weiss form with magnitude appropriate to a $j=7/2$ moment of Yb and a small Weiss temperature[16] $\Theta_W\sim-13$ K, which constrains the effective Kondo temperature appropriate in this high temperature range to be comparably small in magnitude. The resistivity in this temperature range[2] is very high for a metal ($\rho_{dc}\simeq 150\ \mu\Omega$ cm) and together with Hall measurements indicate a very low (hole) carrier concentration.[2] Lowering the temperature through the first order phase transition has dramatic effects on both the spin and charge response. For $T<T_v$, the magnetic susceptibility drops considerably into a temperature independent (Pauli paramagnetic) form, with a magnitude indicating a dramatic increase in the Kondo temperature. In concert the carrier concentration increases markedly and the resistance drops.[2] Extensive experimentation

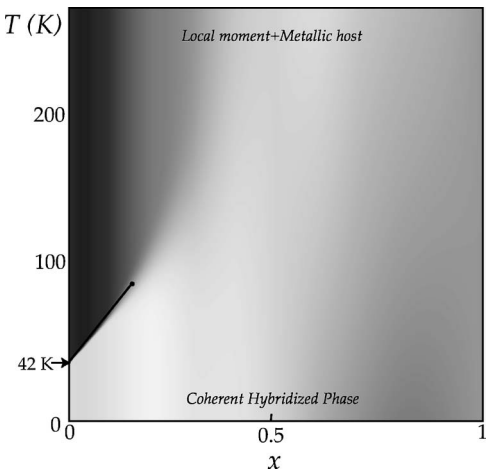

FIG. 1. Schematic phase diagram of $YbIn_{1-x}Ag_xCu_4$. Lighter shading indicates a larger T_K. A line of phase transitions at low x, involving an abrupt change in T_K, ends at a critical point near $x=0.2$.

has revealed substantial changes in specific heat,[8,16–18] elastic constants,[6,17] single-particle (photoemission),[19–23] two-particle (optical),[24–27] and neutron[5] spectroscopies.

Changes associated with the phase transition in $YbInCu_4$ are generally interpreted as an effective screening of the localized Yb $4f$ moments in the low temperature phase. This is associated with an order of magnitude increase in Kondo coupling scale ($T_K \sim 20$ K for $T > T_v$; $T_K \sim 300$ K for $T < T_v$). Universal scaling observed[4,28] in the B-T plane was shown[29,30] to be consistent with the scenario of a transition-induced screening of the Yb moment. Doping Ag on the In site serves to stabilize the low temperature phase, driving the phase transition temperature upward.[2] Experimentally, the transition becomes less sharp with doping and the transition disappears[2] beyond a critical concentration of about $x_c \simeq 0.2$. For the highest x values (0.75 and 1), the samples display behavior typical of heavy fermion systems, where coherent heavy metallic quasiparticles responsible for the low energy physics have an enhanced mass as high as $m^* \simeq 50m_e$. The intermediate x values, e.g., 0.3 and 0.5, offer a view of the phenomenology of a crossover region between the unusual temperature dependence of the low x region and the more well-studied correlated electron physics of the high x, heavy fermion regime.

Much of the phenomenology of $YbIn_{1-x}Ag_xCu_4$ is reflective of periodic Anderson model (PAM) physics, however, the phase transitions associated with the PAM (Ref. 31) (which involve a competition between magnetic order and Fermi liquid phases) occur in a region of weak coupling. This region is far from the mixed-valent fixed point, where the coupling is strong or intermediate, and these transitions are therefore unlikely to be directly relevant to $YbIn_{1-x}Ag_xCu_4$. The PAM, in the region of intermediate to strong coupling, exhibits gradual crossover to a coherent state as temperature is reduced. It does not, to our knowledge, include phase transitions like those found in $YbInCu_4$. One may therefore ask whether the line of phase transitions occurring at low x, which are electronic and not structural in origin, imply the need for an additional interaction term in the minimal model Hamiltonian for $YbIn_{1-x}Ag_xCu_4$ beyond those normally included in the PAM. An intriguing possibility is that electron-electron interactions, which cause phase transitions in Mott-Hubbard systems, may play a role in $YbIn_{1-x}Ag_xCu_4$. Investigations along these lines have been pursued by Giamarchi *et al.*[32] and Zlatic and Freericks.[33–35]

In this paper, we present a systematic study of the finite-frequency dynamics of $YbIn_{1-x}Ag_xCu_4$ derived from measurements of the reflectivity of single crystal samples with Ag compositions $x=0$, 0.3, 0.5, 0.75, and 1.0. We study both the x dependence and temperature dependence of the optical signature of the Kondo resonance. The temperature dependence is highly unusual and, to our knowledge, cannot be explained within the context of the PAM suggesting that an additional interaction term may be required. At very low x the Kondo resonance appears abruptly as the samples are cooled; this appearance becomes much more gradual in samples with higher x. In addition to the growth of the Kondo resonance excitation as T is diminished, there is a substantial loss of spectral weight with cooling near 1 eV for low x. In this systematic study we also examine the scaling behavior of the infrared signature of the Kondo resonance excitation, as a function of T_K, at low temperature.

Our measurements cover the frequency range from 40 cm^{-1} to 50 000 cm^{-1} with detailed temperature-dependent data taken between 40 cm^{-1} and 23 000 cm^{-1}. Each sample was mounted into a recess custom-machined into a brass disk. Each disk was polished (minimally) such that a smooth, flat sample surface sits parallel to a similarly flat, polished portion of the brass mounting disk. Ag film was then evaporated on the bare brass surface, creating a reference mirror for use in the temperature-dependent reflectivity measurements. Soon after evaporation, the sample disk was mounted inside a continuous-flow He^4 cryostat with a custom switching mechanism designed to expose either Ag or sample surfaces to the beam. To insure that the reference mirror and sample surface are coplanar and flat, a laser alignment procedure was used on the mounted sample disk. Frequency-dependent spectra were then taken using a combination of Fourier transform and grating spectrometers. At each temperature and composition, spectra were taken for Ag and the sample exposed through the cryostat window and the ratio at each frequency used to determine the reflectivity $R(\omega)$.

In addition to the temperature dependence, room temperature reflectivity spectra were also taken in the range $12\,500\ cm^{-1} < \omega < 50\,000\ cm^{-1}$ with an optical setup which measures absolute reflectivity without the use of a reference mirror. The spectra taken by this method and those spectra taken using the cryostat (and with Ag reference) generally agree well in the region of overlap ($12\,500\ cm^{-1} < \omega < 23\,000\ cm^{-1}$). Through this comparison, we estimate the uncertainty of the absolute value of the reflectivity in the temperature dependent measurements to be less than 1%.

A Kramers-Kronig transform is applied to the measured reflectivity in order to determine the frequency-dependent reflection phase shift.[36,37] The magnitude and phase of the reflectivity are then used in order to determine the dynamical conductivity $\sigma_1(\omega)$ [and the dielectric function $\epsilon_1(\omega)$]. For the purposes of the transform, Hagen-Rubens terminations $[1-R(\omega) \propto \sqrt{\omega}]$ are used below 40 cm^{-1}. At high frequency (above 50 000 cm^{-1}) each reflectivity spectrum is extrapolated to a common value of 0.08 at 120 000 cm^{-1} and then continued as a constant to 200 000 cm^{-1}. Between 200 000 cm^{-1} and 400 000 cm^{-1}, an ω^{-2} form is used for $R(\omega)$ to represent the nonconstant reflectivity expected as a result of deep core level excitations.[37] At still higher frequencies, the free-electron form ω^{-4} is assumed.

We have experimented with a number of termination protocols including other common values and coalescence frequencies as well as constant extrapolations above 50 000 cm^{-1}. These show convincingly that our results regarding trends in the x and T_K dependence of $\sigma_1(\omega)$ below 10 000 cm^{-1} are not significantly influenced by any of the extrapolations above 50 000 cm^{-1}. The conductivity above 10 000 cm^{-1} but below 20 000 cm^{-1} is influenced by the detailed extrapolation by about 5% for reasonable extrapolation protocols.

In $YbInCu_4$, where a first order phase transition occurs at finite temperature, we have been careful to control the potential hysteresis effects[2,6] usually associated with first order

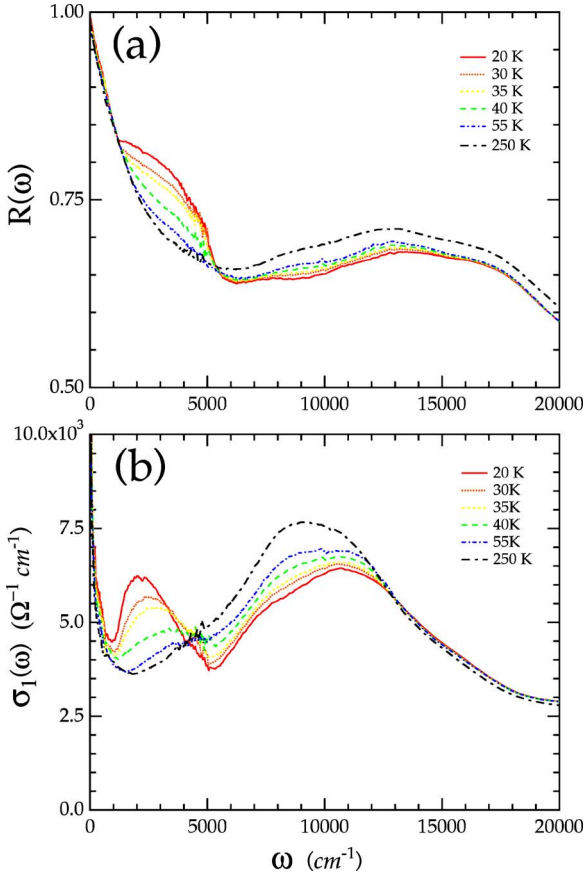

FIG. 2. (Color online) The reflectivity (a) and the real part of the optical conductivity (b) of $YbInCu_4$ are shown at 20, 30, 35, 40, 55, and 250 K.

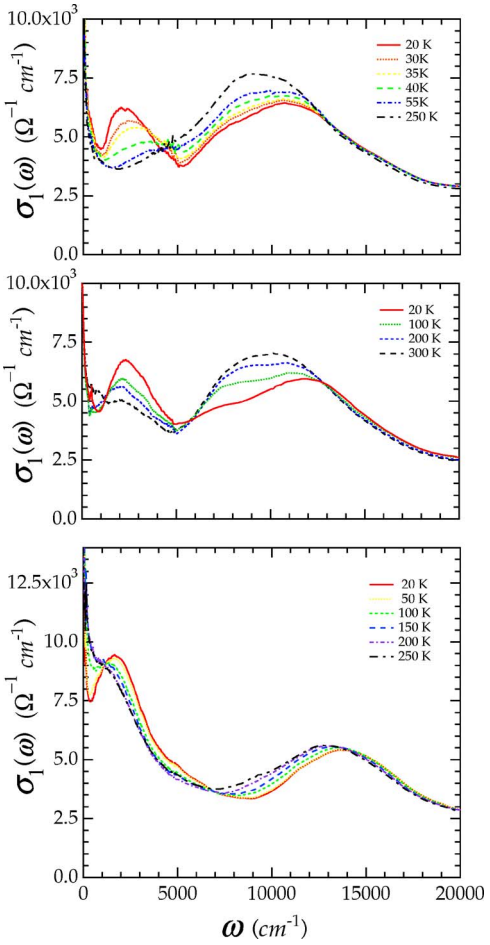

FIG. 3. (Color online) The temperature dependence of $\sigma_1(\omega)$ of $YbIn_{1-x}Ag_xCu_4$ is shown for the low and intermediate x values 0, 0.3, 0.5.

phase transitions by keeping the thermal cycling through the phase transition to a minimum while collecting the optical data. We found that hysteresis effects are observable in the infrared spectrum, and are especially pronounced in the frequency range $1000 < \omega < 7000$ cm^{-1} (see Fig. 2). For this reason, our data for several ranges were retaken on fresh samples.

I. RESULTS

Figure 2 shows the reflectivity and conductivity $\sigma_1(\omega)$ of $YbInCu_4$ as a function of frequency at temperatures below and above the $T_v \simeq 42$ K phase transition temperature. The 250 K conductivity spectrum includes a relatively narrow free carrier contribution seen below about 1000 cm^{-1} associated with the presence of mobile carriers. This interpretation is consistent with Hall[38] and resistivity measurements.[2] In addition there is a broad peak, centered near about 9000 cm^{-1} which we associate with an important Fermi-level to f level interband transition, as discussed in Sec. V. As temperature is reduced, there is a significant decrease in conductivity in this interband region ($\omega \sim 9000$ cm^{-1}), and below 55 K there is an additional complementary increase in the conductivity at lower frequency. By 20 K this lower energy feature has evolved into a well-developed peak centered at $\omega \simeq 2000$ cm^{-1}. The connection between this peak and the physics of hybridization is an important theme of this paper.

Figure 3 shows the temperature dependent behavior of $\sigma_1(\omega)$ for our samples with low and intermediate x values (i.e., for $x=0$, 0.3, and 0.5). The low x samples show an increase of $\sigma_1(\omega)$ around 2000 cm^{-1} as T is lowered, accompanied by a decrease of spectral weight at higher frequency (in the vicinity of 8000–10 000 cm^{-1}). This low-x temperature dependence is markedly different from the high-x temperature dependence shown in Fig. 4. In the high x region the conductivity shows behavior more typical of a heavy fermion system. The temperature dependence has a smaller overall magnitude and is more gradual, and spectral weight is approximately conserved below about 6000 cm^{-1} (0.75 eV). The $x=0.5$ sample provides an intermediate case, with aspects of both the low and high frequency temperature dependence evident. Figures 3 and 4 thus provide a view of the unusual temperature dependence of $YbIn_{1-x}Ag_xCu_4$ and its interesting evolution as a function of x.

We turn now to the x dependence of the infrared and optical conductivity at low temperature, as shown in Fig. 5 (also see Table I). Although the low-energy peak shifts in frequency as a function of x, and indeed that is major part of our study, it is convenient to refer to it as the 2000 cm^{-1} peak ($\simeq 0.25$ eV). As shown in Fig. 5, this peak undergoes a com-

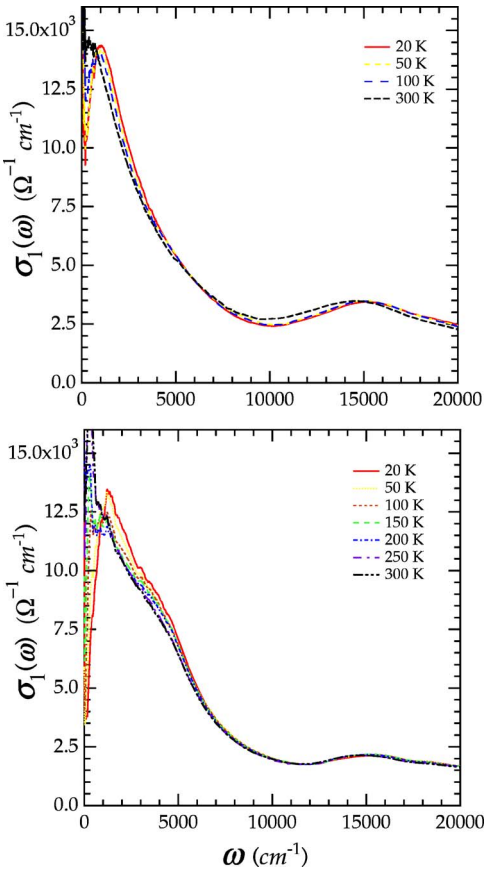

FIG. 4. (Color online) The temperature dependence of $\sigma_1(\omega)$ of $YbIn_{1-x}Ag_xCu_4$ is shown (the high x values 0.7 and 1.0).

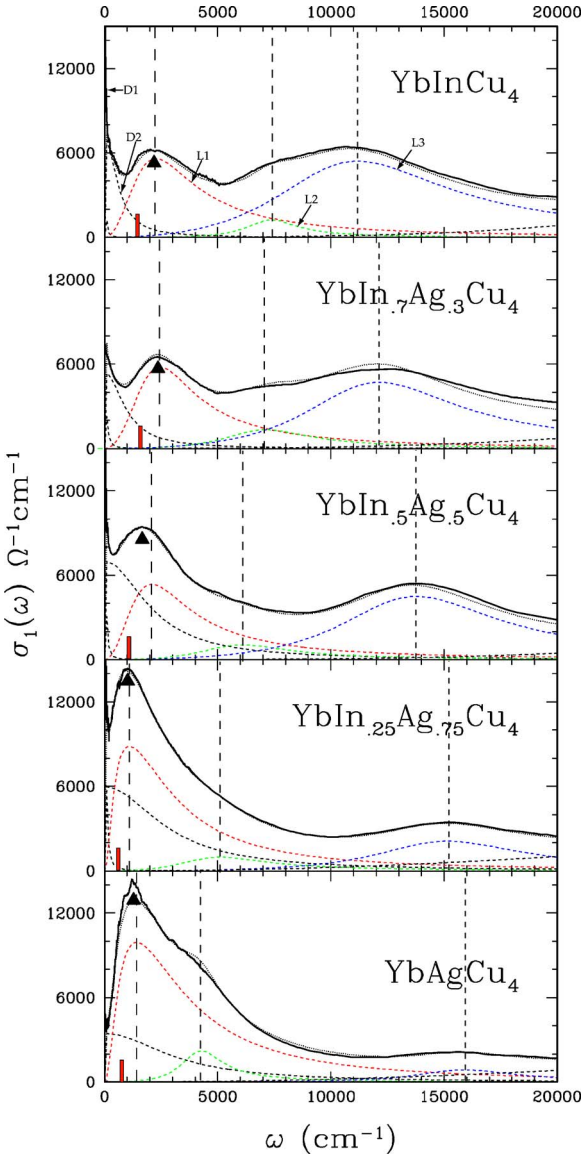

FIG. 5. (Color online) Infrared conductivity $\sigma_1(\omega)$ versus ω at 20 K for the five x values studied. Also shown are the components of a Lorentzian-Drude fit. The identification of L1, L2, and L3 is addressed in Fig. 12 and the accompanying discussion. The dashed vertical lines correspond to the center frequencies of the fit components for each x.

plex shifting behavior as x is increased, blueshifting slightly when $x=0.3$, then redshifting upon further doping, reaching a minimum peak frequency when $x=0.75$, before blueshifting again as x continues to 1. The strength of this feature is also influenced by x in a nontrivial way, discussed further below.

At higher frequency, the large hump feature centered on 11 000 cm^{-1} in $YbInCu_4$ monotonically blueshifts and decreases in overall strength as x is increased. Further, inflection points around 6000 cm^{-1} and 9000 cm^{-1} redshift slightly upon doping to the $x=0.3$ and $x=0.5$ systems. These inflection points are not discernable for $x=0.75$, but reappear at low frequency (3000 cm^{-1} and 5500 cm^{-1}) in the $x=1$ system.

The x-dependent profiling of the low temperature conductivity is an important part of our experimental results, allowing clear identification of systematic changes of the low temperature electrodynamics as a function of an external control parameter. The discussion begins with the identification of systematic trends in the 2000 cm^{-1} feature followed by discussions of temperature dependence and interband features in later sections.

Figure 6(a) shows the frequency of the 2000 cm^{-1} feature versus x as determined in two ways. The black triangles mark the frequency of the peak in $\sigma_1(\omega)$ (also marked in Fig. 5). Alternatively, a threshold frequency can be extracted from a fit of the conductivity to a calculation based on the low energy dispersion of the periodic Anderson model (PAM), discussed below.

In addition to examining the frequency of the peak as a function of x, we can also look at the strength of the 2000 cm^{-1} feature. We quantify this characteristic through the spectral weight, defined as the integrated intensity of $\sigma_1(\omega)$ over a low frequency interval as follows:

$$n(\omega) = \frac{2m}{\pi e^2}\int_{0^+}^{\omega} \sigma_1(\omega')\mathrm{d}\omega', \qquad (1)$$

where m represents a bare band mass. The lower limit is chosen to be nonzero ($0^+=50$ cm^{-1}) in order to exclude from the strength estimate the comparatively minute contribution of the free carrier (Drude) response. The upper limit of integration is chosen to encompass the 2000 cm^{-1} peak without

TABLE I. Parameters of the fitting procedure in Fig. 5. Temperature units are K, all other units are cm^{-1}.

		DN			DW			L1			L2			L3		
x	T	ω_0	Γ	ω_p	ω_0	Γ	ω_p	ω_0	Γ	ω_p	ω_0	Γ	ω_p	ω_0	Γ	ω_p
0	20	0	20	6000	0	640	16400	2271	3790	35600	7386	2814	14427	11181	9407	55187
	30	0	37	5700	0	735	16900	2555	4350	36150	7525	2840	14427	11121	9290	54677
	35	0	47	5600	0	795	17170	2717	4770	36620	7595	2870	14427	11092	9225	54303
	40	0	72	5690	0	923	17460	3156	6776	40220	7783	2994	14427	11105	8898	51764
	55	0	111	5953	0	1246	19003	3938	8733	41319	7782	2990	14427	10970	8650	50575
	250	0	103	6000	0	2125	23500	4800	7615	36500	7667	2977	14427	10390	8360	52670
0.3	20	0	98	5200	0	998	17960	2452	3588	35240	7444	4729	22962	12134	8434	48746
	100	0	112	5955	0	1145	17537	2365	3975	33942	7532	3899	23642	11778	8737	50240
	300	0	100	5272	0	2912	30753	2922	3376	18017	7690	4461	26025	11095	8613	52174
0.5	20	0	60	6547	0	2181	30200	2097	3702	34470	6094	4789	17374	13780	8633	48180
	250	0	60	1528	0	555	19631	1600	4034	41760	7654	6766	19510	13150	8801	48180
0.75	20	0	66	8370	0	2872	32074	1099	3295	41770	5132	4746	16589	15152	7919	31600
	300	0	58	10745	0	6678	40510	297	3220	52344	5504	5066	17081	14511	8366	33291
1	20	0	10	2306	0	3274	25998	1421	3891	48064	4281	2283	17318	15927	5493	16784
	250				0	350	14896	667	3600	49405	3875	3843	25341	15568	5267	16561

including the x dependence of the high frequency interband contributions. Neither integration limit is critical; in fact a lower limit of 0 and upper limits anywhere between 3000 cm^{-1} and 8000 cm^{-1} produce a similar x dependence. [$n(4000\ cm^{-1})$ and $n(6000\ cm^{-1})$ are shown in Fig. 6(c)].

As an alternative to this simple integral calculation of the strength, we can fit the complex conductivity ($\sigma=\sigma_1+i\sigma_2$) with a sum of Lorentzian and Drude response functions to[36,37]

$$\sigma(\omega)=\sum_j \frac{\omega_{P,j}^2}{4\pi}\frac{\omega}{i(\omega_j^2-\omega^2)+\omega\Gamma_j}. \quad (2)$$

The constituents of the fits include one narrow Drude (D1, $\Gamma\sim 10-40\ cm^{-1}$) contribution to represent the free carrier peak, a wide Drude (D2, $\Gamma>800\ cm^{-1}$), and a Lorentz oscillator (L1) in the vicinity of the 2000 cm^{-1} feature which, as we discuss below, relate to the Kondo resonance. There are in addition two Lorentz oscillators (L2 and L3, around 7300 cm^{-1} and 11 000 cm^{-1} for $x=0$) to represent the infrared interband conductivity, and two wide Lorentz oscillators at ultraviolet frequencies ($\omega>30\ 000\ cm^{-1}$) representing the conductivity in that range. These fit components are labeled in Fig. 5.

Previous work[39] has explicitly demonstrated that the calculated line shape of the optical signature of the Kondo resonance is intrinsically non-Lorentzian, and furthermore demonstrated the viability of fits which combine Drude and Lorentz terms to represent the Kondo resonance. The combination of the contributions D2 and L1 reasonably fit the conductivity in the range of the 2000 cm^{-1} peak. The strength from that combination is shown by the triangles in Fig. 6(c). This determination of the strength exhibits an x dependence similar to the simpler integral representations of the strength. This makes one confident that the n versus x dependence shown here is an essential characteristic of the data, and independent of any of the detailed choices we have made in the analysis. n determined by the methods discussed here is presented in Fig. 6(c).

It is interesting to compare the x-dependent trends inferred from previously published thermodynamic measurements with those from our optical data. Figure 6(b) shows the Kondo temperature of the low-T phase $YbIn_{1-x}Ag_xCu_4$ as deduced by Cornelius *et al.*[3] from fitting the measured magnetic susceptibility to the numerically calculated result of the $j=\frac{7}{2}$ Coqblin-Schreiffer model.[3,40] Figure 6(d) shows that the trend in the x dependence of $\chi(T=0)$[57] generally agrees with the corresponding trend in the Sommerfeld coefficient γ, implying a Wilson ratio within 10% of the value $\left(\mathcal{R}=\frac{8}{7}\right)$ expected for a $j=\frac{7}{2}$ Anderson impurity.[3,41] Thus the T_K values inferred from the susceptibility analysis reasonably represent the effective energy scale relevant to the onset of strong-coupling Kondo physics within the low temperature phase.

The complicated x dependence of T_K is not understood, and may be the result of an interplay of band structure, chemical pressure, screening, disorder, and other many-body effects. While resolving the detailed cause of this complex x dependence presents a subject for future work, our focus here is the relationship between the x dependence of T_K and that of the optical data; the similar form of the x dependent electrodynamic [Figs. 6(a) and 6(c)] and thermodynamic quantities [Figs. 6(b) and 6(d)] indicates a common source. We show below that this is rooted in the strongly correlated electron physics of hybridization.

II. MODELING, INFRARED CONDUCTIVITY

We can make progress toward eliciting the relationships suggested in Fig. 6 by examining an interpretation of the 2000 cm^{-1} feature in the context of the periodic Anderson

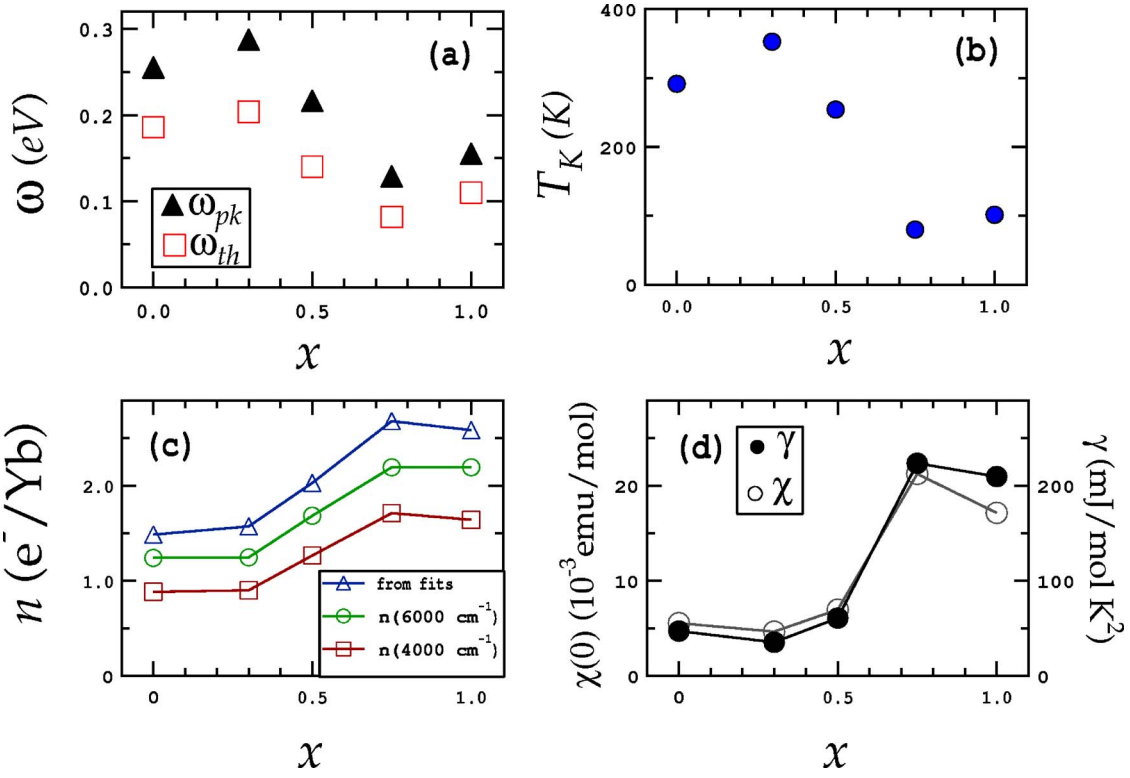

FIG. 6. (Color online) (a) The characteristic frequencies, ω_{pk} (triangles) and ω_{th} (boxes), and (b) the Kondo temperature as a function of x. (c) The spectral weights, $n(4000\ \mathrm{cm}^{-1})$ (boxes) and $n(6000\ \mathrm{cm}^{-1})$ (circles) and the results of a combined Drude/Lorentz fitting (triangles) of the low frequency conductivity. (d) The low temperature susceptibility (open circles) and Sommerfeld coefficient (solid circles) as a function of x. T_K in (b) is related to $\chi(0)$ in (d). Spectral weights are computed assuming a band mass of $4m_e$.

model (PAM). Complementary to the work of other authors,[33,34,39,42–44] which focus the rigorous techniques of many body theory directly toward the underlying Hamiltonian, we will use a simplified approach based on effective low energy (near-E_F) PAM dispersion relations.[41,45] These dispersion relations (ϵ^+ and ϵ^- in Fig. 7) provide the basis for a simple unifying picture in which much of the low energy phenomenology of heavy fermion materials can be viewed, including the mass enhancement, aspects of magnetism, and transport measurements.[46,47] In Fig. 7, the vertical extent of the plot is of order 1 eV and the (singly occupied) f-electron level is below the bottom plot boundary. The light dashed lines indicate the bare (unhybridized) conduction electron dispersion.

In a system with no hybridization, the conduction electrons are the dominant influence on the transport properties such as thermopower and resistivity, while at the same time provide a temperature-independent Pauli-paramagnetic contribution to the magnetic susceptibility. The f electrons, on the other hand, are localized and as a result contribute very little to the transport properties, but play a major role in magnetism, contributing a Curie $1/T$ term to the susceptibility. Inclusion of the hybridization and onsite Coulomb repulsion terms leads to fundamental departure from this independent particle picture, in which the eigenstates become nontrivial admixtures of the states of f and conduction electron character.

For energies far from the chemical potential, the effect of the interaction and hybridization is to provide a channel for relaxation of the conduction states, i.e., a broadening of the spectral function along the dispersion curves, however, at lower energies renormalization opens the Fermi surface, and the bands flatten to accommodate the f-electron weight projected up to the Fermi level as $k_F^{(bare)} \rightarrow k_F$. As we have discussed previously,[25] the reorganization of the bands in the vicinity of the Fermi level due to many body interactions characterized by the parameter $\tilde{V}$ leads to narrow peak in the density of states, called the Kondo, or Abrikosov-Suhl, resonance,[58] which is central to the understanding of heavy

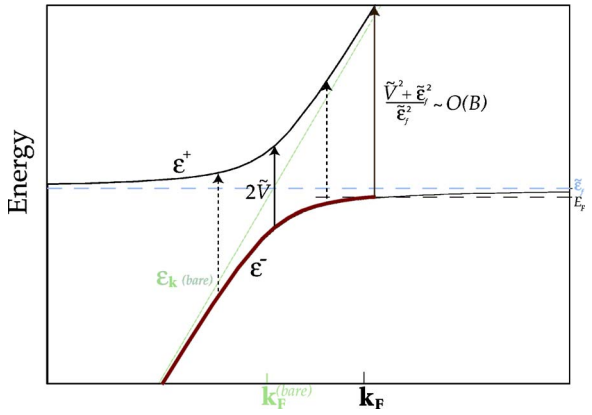

FIG. 7. (Color online) The PAM dispersion relations. Vertical arrows indicate possible optical transitions. The horizontal dashed lines represent E_F and $\tilde{\epsilon_f}$. The light diagonal line represents the unrenormalized dispersion of the conduction carriers.

fermion and mixed-valent phenomenology.[41,42,48]

As discussed by us previously,[25] this renormalization creates the possibility for vertical transitions from filled states below E_F, across a *direct* gap, and into unoccupied levels above E_F, (see the vertical arrows in Fig. 7) at a threshold energy of[46,49–52]

$$2\tilde{V} = 2\sqrt{T_K B}, \tag{3}$$

where $\tilde{V}$ is the hybridization strength renormalized by the onsite f-electron repulsion and B is a model parameter associated with the (conduction electron) bandwidth. At threshold, the nesting condition for the upper and lower bands is met ($\nabla_{\mathbf{k}}\epsilon^+ = \nabla_{\mathbf{k}}\epsilon^-$), leading to a very high quasiparticle joint density of states and a strong peak in the infrared conductivity.[25]

At frequencies larger than the threshold frequency there are two distinct contributions to the conductivity: one originating from levels inside the unrenormalized Fermi surface ($k_<$ below); the other from the states occupied as a result of renormalization, i.e., outside the unrenormalized Fermi surface ($k_>$ below). An example of two such transitions with the same frequency ω are indicated by dashed arrows in Fig. 7. Transitions involving both of these sets of quasiparticles are important and must be counted independently in the determination of the total optical conductivity, as discussed further below.

In addition to the threshold frequency, another, higher frequency scale appears which is relevant to the electrodynamic response. This higher frequency scale corresponds to the vertical transition (see the long arrow in Fig. 7) which occurs from states *on* the Fermi surface (i.e., the locus of points which divides the set of occupied and unoccupied **k** states). Vertical transitions involving higher **k** states cannot occur because both initial and final states are unoccupied when $k > k_F$, and hence one expects a drop in the conductivity at this frequency. For a linearly dispersing conduction band, direct calculation reveals that the frequency of the last allowed transition is equal to

$$\Omega_{FS} = \frac{\tilde{V}^2 + \tilde{\epsilon}_f^2}{\tilde{\epsilon}_f}. \tag{4}$$

The identification of $\tilde{\epsilon}_f$ with T_K (discussed further below), together with Eq. (3) implies that this scale is of the order of the conduction electron bandwidth, B. For high energy transitions, band edge final states can be reached and the linear approximation to the conduction band is likely to become poor. Quasiparticle transitions in this frequency range may be influenced by the details of the underlying band structure.

As we showed previously,[25] one can calculate a model conductivity via a Kubo-Greenwood approach in a two-band context, in which case one obtains

$$\sigma_{pam}(\omega) = \frac{2\ e^2|\mathbf{p}_{+,-}|^2}{m^2|\nabla\epsilon_{k_F}|^3\pi}\frac{(E_F+\tilde{\epsilon}_f)^2+\omega^2-4\tilde{V}^2}{\sqrt{\omega^2-4\tilde{V}^2}} \tag{5}$$

for $2\tilde{V} < \omega < \frac{\tilde{V}^2+\tilde{\epsilon}_f^2}{\tilde{\epsilon}_f}$ and

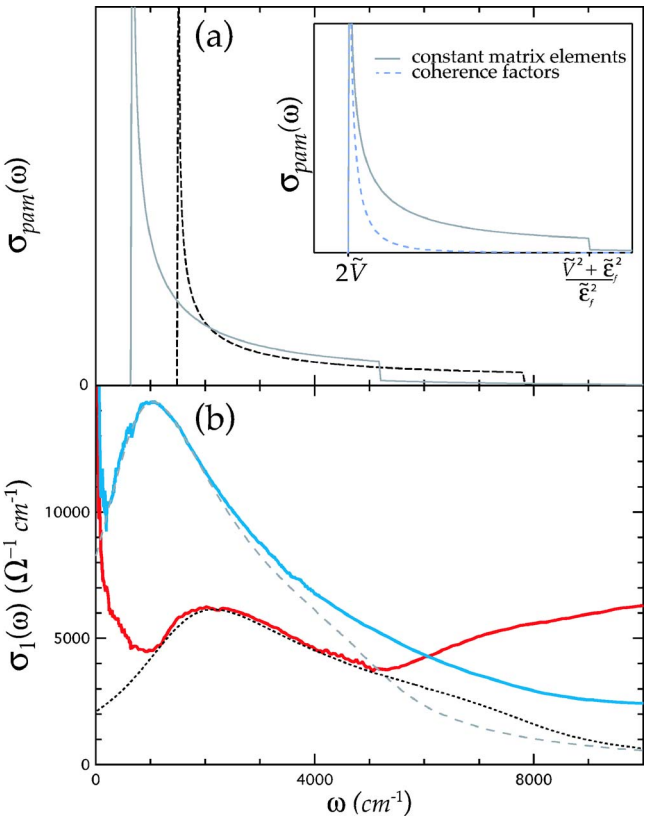

FIG. 8. (Color online) (a) The idealized conductivity [Eqs. (5) and (6)] for $\tilde{V}$=93 meV and $\tilde{\epsilon}_f$=9 meV (solid) and $\tilde{V}$=40 meV and $\tilde{\epsilon}_f$=2.5 meV (dashed). The inset contrasts the lineshapes derived with constant matrix elements $|\mathbf{p}_{+,-}|$ [Eqs. (5) and (6)], and those with the coherence factors discussed in the text. (b) The same idealized conductivity curves as (a), Lorentzian broadened with widths Δ_0=0.16 eV and $\Delta_{0.75}$=0.125 eV for comparison to the measured conductivity of $YbIn_{1-x}Ag_xCu_4$ with x=0 and x=0.75, respectively.

$$\sigma_{pam}(\omega) = \frac{e^2|\mathbf{p}_{+,-}|^2}{m^2|\nabla\epsilon_{k_F}|^3\pi}\frac{(E_F+\tilde{\epsilon}_f-\sqrt{\omega^2-4\tilde{V}^2})^2}{\sqrt{\omega^2-4\tilde{V}^2}} \tag{6}$$

for $\omega > \frac{\tilde{V}^2+\tilde{\epsilon}_f^2}{\tilde{\epsilon}_f}$, where $|\mathbf{p}_{+,-}|$ is the matrix element for transitions between the two bands under consideration. Figure 8(a) shows this lineshape for two sets of $\tilde{V}$ and $\tilde{\epsilon}_f$ values. The dramatic onset of the model optical conductivity occurs at the threshold frequency given by Eq. (3). The upper cutoff occurs at the frequency given by Eq. (4) as discussed above, and is associated with end of occupied states in the lower coherent band, ϵ^-, at k_F (c.f. Fig. 7). The possible association of this cutoff with the experimental feature, L2, is discussed in Sec. V, which focuses on the behavior of the high frequency transitions.

The lineshape generated by these considerations is extremely sharp and a meaningful comparison with the data requires addressing the effects of relaxation. To this end, we convolute this idealized lineshape with a Lorentzian function, keeping the half width Δ as an adjustable parameter when performing fits to the measured conductivity. Examples

of fits produced using this procedure are shown in Fig. 8(b).

The broadening parameter Δ addresses the finite width of the spectral function along the dispersion curves of Fig. 7, and therefore provides a measure of the statistical time over which a typical quasiparticle decays. The numerical values for Δ obtained from our fits range from 0.12 to 0.17 eV, with an associated time scale for decay in the range $\tau=\hbar/\Delta=5.4$ ps to 3.8 ps, respectively. These lifetimes estimates are in good agreement with the quasiparticle lifetime of members of this class of materials ($YbAgCu_4$), as measured directly by Demsar *et al.* in pump probe experiments[53] of electron-hole relaxation lifetime. The extraction of a comparable lifetime from this analysis of conductivity data is a meaningful consistency check on the method developed here.

We now take a moment to consider the possible influence of **k**-dependent matrix elements associated with the composite nature of the hybridized quasiparticles on the electrodynamic response. The hybridizing quasiparticles are composite admixtures of excitations with both *f* and conduction electron character. The regions of the dispersion which are flatter correspond to quasiparticles with a large amplitude of *f* admixture whereas regions which follow more closely the bare conduction dispersion are dominated by conduction character. Generally speaking transitions among the bare states are not all equally probable (i.e., $|\mathbf{p}_{cc}| \neq |\mathbf{p}_{cf}| \neq |\mathbf{p}_{ff}|$). Thus one expects that the optical transition rate for quasiparticles may exhibit some dependence on **k**, which goes beyond our earlier assumptions.

One can obtain a relatively simple model with **k** dependence by assuming transitions among bare states only occur between conduction electron initial and final states ($|\mathbf{p}_{cc}| \neq 0, |\mathbf{p}_{cf}| = |\mathbf{p}_{ff}| = 0$), and using that to calculate the transition rates between the hybridized quasiparticle bands. To model the nonconstant admixture of states, we use the coherence factors of the resonant level model[47,50] (also known as Fano-Anderson[54]),

$$u_{\mathbf{k},\sigma} = \frac{1}{\sqrt{1+\left(\frac{\tilde{V}}{\tilde{\epsilon}_f - \epsilon^+}\right)^2}}, \quad v_{\mathbf{k},\sigma} = \frac{1}{\sqrt{1+\left(\frac{\tilde{V}}{\tilde{\epsilon}_f - \epsilon^-}\right)^2}}. \tag{7}$$

The calculation of the optical conductivity is then altered because the JDOS integral [Eq. (4) from Hancock *et al.*[25]] picks up a factor $u^2_{\mathbf{k},\sigma} v^2_{\mathbf{k},\sigma} = \tilde{V}^2/\omega^2$ associated with these coherence factors. One thus obtains a model conductivity similar to Eqs. (5) and (6), but with $|\mathbf{p}_{+,-}|^2$ replaced by $|\mathbf{p}_{cc}|^2 \tilde{V}^2/\omega^2$. The most significant effect of the inclusion of coherence factors is that the conductivity at high frequency should fall to zero much more quickly than in the constant matrix element case.[50] The line shapes with and without coherence factors are contrasted in the inset of Fig. 8(a).

This approach may be too nuanced because in a general mixed valent system, bare *f*-to-conduction state transitions can be appreciable, and in fact are expected to be important in $YbIn_{1-x}Ag_xCu_4$. This is because the conduction band states are derived primarily from Cu-In-Ag *p* and *d* orbitals,[26] whereas the *f* electrons sit on Yb sites. This physical displacement between the underlying orbital states is manifest in the banded states through nonvanishing dipole transition matrix elements, $|\mathbf{p}_{fc}|$.[50] Thus, in $YbIn_{1-x}Ag_xCu_4$, transitions involving the flatter portions of the quasiparticle dispersion, which are dominated by *f*-like character, *can* be expected to provide a considerable contribution to the optical strength, thus we feel that Eqs. (5) and (6) are more applicable to $YbIn_{1-x}Ag_xCu_4$.

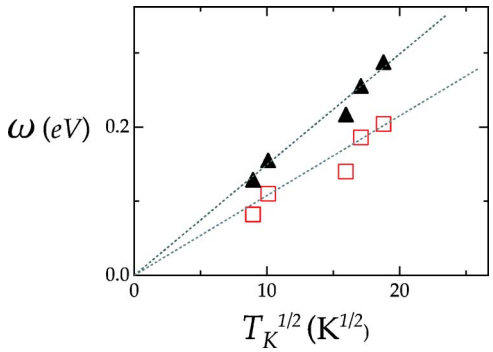

FIG. 9. (Color online) Plot of ω_{pk} and ω_{th} versus $\sqrt{T_K}$. The dotted lines represent Eq. (3) and the slopes are 1.6 eV$^{1/2}$ and 1.1 eV$^{1/2}$.

III. DISCUSSION, T_K SCALING

We now analyze the *x* dependent frequency of the 2000 cm^{-1} feature [Fig. 6(a)], and its relationship to the Kondo temperature T_K [Fig. 6(b)]. Figure 9 shows ω_{pk}, the maximum of the conductivity, and the threshold frequency ω_{th}, determined from the fit described above, plotted versus the square root of the Kondo temperature. The complex *x* dependence of ω_{th} and ω_{pk} (Fig. 6) simplifies considerably when we plot these quantities as a function of T_K (Fig. 9). The emergence of a functional relationship between these quantities implies that the frequency of the 2000 cm^{-1} peak is controlled by the same physics that underlies the thermodynamic behavior. The square root dependence is evidence that hybridization physics plays a dominant role.

With that in mind, the modeling developed in the previous section can be used to extract an estimate for the band parameter *B* [Eq. (3)] by associating the threshold frequency, ω_{th}, with its PAM value, $2\tilde{V}$. The slope of the line through the ω_{th} values in Fig. 9, together with Eq. (3), directly gives $B=0.30$ eV. This value of *B* reflects the rate at which the frequency increases with T_K. This can be compared with expectations based on density of states, as well as the rate at which the strength decreases with T_K, as discussed below.

As shown previously,[25] one can integrate σ_{pam} in closed form to obtain

$$n_{pam} \simeq \frac{4|\mathbf{p}_{+,-}|^2 k_F}{\pi^2} \ln\left(c\sqrt{\frac{B}{T_K}}\right). \tag{8}$$

This is essentially the area under the curves of Fig. 8(a). Figure 10(a) shows a least squares fit of this logarithmic scaling relationship between T_K and n_{pam}.

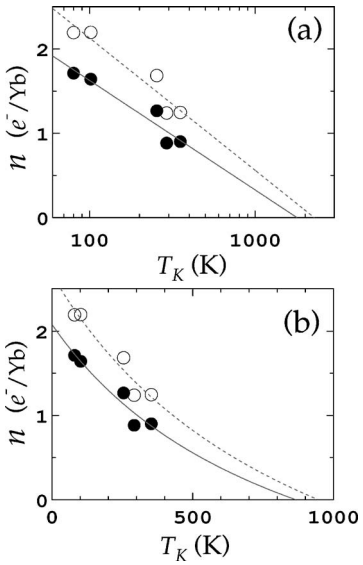

FIG. 10. Scaling relations for the strength of the 2000 cm^{-1} feature with T_K. Dark circles represent $n(4000\ cm^{-1})$ and open circles represent $n(6000\ cm^{-1})$. (a) Shows the result of fitting the measured dependence with Eq. (8), and (b) shows the same data fit with Eq. (12).

The factor c relates the renormalized f level position at low energies and the Kondo temperature, T_K. The value of c is unambiguous in the Fermi liquid theory of the $N(=2j+1)$-fold degenerate Anderson impurity model where,

$$\tilde{\epsilon}_f = \frac{T_K}{c} = k_B T_L \frac{N^2 \sin(\pi/N)\cos(\pi/N)}{\pi(N-1)}, \tag{9}$$

and[59]

$$T_K = w_N T_L. \tag{10}$$

w_N is the generalized Wilson number[41] given by

$$w_N = \frac{e^{1+C-(3)/(2N)}}{2\pi\Gamma\left(1+\frac{1}{N}\right)}. \tag{11}$$

For the $j=\frac{7}{2}$ moment of Yb, $N=8$ and $c \simeq 0.66$.

Using this value of $c \simeq 0.66$ and fitting the measured result to Eq. (8) gives $B=0.35$ eV and 0.45 eV for $n(4000\ cm^{-1})$ and $n(6000\ cm^{-1})$ [Eq. (1)], respectively. We consider these to be a reasonable agreement given the simplicity of our approach. These values of B, which are determined by the amount that n goes up when T_K goes down, are similar in size to our previous estimate of the parameter $B=0.30$ eV determined from the amount that ω_{th} goes down as T_K goes down. Therefore, in addition to the agreement of experiment and theory regarding the *direction* of the T_K dependence of n and ω_{th}, the *sensitivity* of the dependence of n and ω_{th} on T_K are in reasonable agreement *with each other*. In addition, the numerical values for B are reasonable bandwidths for the InAgCu d-orbital derived band states[26,55,57] of $YbIn_{1-x}Ag_xCu_4$. Thus we conclude that the observed dependences of both n and ω_{th} on T_K is consistent with the predictions of the periodic Anderson model in magnitude as well as direction.

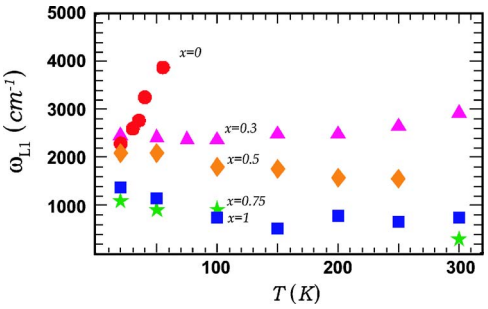

FIG. 11. (Color online) The frequency of the Kondo resonance excitation (L1) is shown as a function of temperature for each value of x for $YbIn_{1-x}Ag_xCu_4$.

An alternative strength estimate can be made using the coherence factor model of the conductivity, shown in detail above. In that case, we replace $|\mathbf{p}_{+,-}|^2$ of Eq. (5) of Hancock *et al.*[25] by $|\mathbf{p}_{cc}|^2\tilde{V}^2/\omega^2$ and integrate to obtain an alternate result for the theoretical strength

$$n_{pam} = \frac{|\mathbf{p}_{cc}|^2 k_F}{\pi^2} \frac{c^2 B - T_K}{c^2 B + T_K}. \tag{12}$$

Again using $c=0.66$, fits to the data would yield B estimates 0.17 and 0.19 eV, for $n(4000\ cm^{-1})$ and $n(6000\ cm^{-1})$, respectively. These values are in order-of-magnitude agreement with the band parameter estimates made above. This functional form is fit for comparison to the data in Fig. 10(b). However, as discussed at the end of Sec. II, the f-to-conduction electron transitions are made allowed in this system and so the calculation which includes these, represented by Eq. (8) is probably more appropriate for $YbIn_{1-x}Ag_xCu_4$.

IV. TEMPERATURE DEPENDENCE AND SUM-RULES

The previous sections focus on the x dependence of the "2000 cm^{-1}" feature and show that the scaling of both its strength and frequency are consistent with predictions based on PAM dispersion relations. This analysis provides a strong basis for identifying this feature as a Kondo resonance transition, as illustrated in Fig. 7. Here we look at the *temperature dependence* of this Kondo resonance transition. Figure 11 shows peak frequencies of this transition, taken as the center frequency of the associated Lorentzian (L1) from the fitting described in Sec. I. These are shown as a function of temperature for each value of x. For $x=0$, the large blueshift can partly be attributed to an increase in damping in combination with the asymmetric line shape. However, this alone cannot account for the entire blueshift below 50 K. While there is uncertainty in the fitting, particularly at higher temperatures, these data indicate an increase in frequency with temperature at $x=0$, and a possible decrease of the transition frequency with temperature up to about 150 K for $x=1$.

Understanding the fundamental origins of this temperature dependence is beyond the scope of the present work,

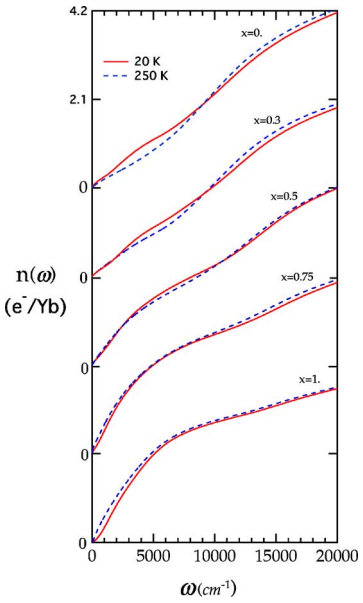

FIG. 12. (Color online) $n(\omega)$, the integral of $\sigma_1(\omega)$, is shown at 20 K and 250 K for five x values. The curves for different x all have the same vertical scale; each pair is offset from the preceding one by an amount corresponding to 2.1 carriers per Yb for a mass of $4m_e$, as shown.

however, it seems potentially interesting and suggests a problem to be addressed by future theoretical work. Thermodynamic measurements[3] indicate that the Kondo scale is essentially constant below the phase transition temperature, thus the apparent change in the Kondo resonance transition energy with temperature is puzzling and indicates physics beyond the $\sqrt{T_K B}$ scaling. Addressing the temperature-dependent behavior of this system and understanding the origins of the phase transition remain important goals for future theoretical work.

Figure 12 shows the integral of $\sigma_1(\omega)$ from 0 to ω at 20 and 250 K. This sum-rule related quantity, $n(\omega)$ (the infrared spectral weight) evolves in interesting ways as a function of T and x. At the high x values, represented by 1.0 and 0.75, it rises rapidly below about 5000 cm^{-1} and then less rapidly above about 7000 cm^{-1} (0.9 meV). For the low x values, 0 and 0.3, the rate of increase of $n(\omega)$ with ω is more uniform. The composition $x=0.5$ provides an intermediate case which does not fit neatly into either category.

These behaviors reflect the underlying differences in the nature of $\sigma_1(\omega)$ at different x values. For high x, $\sigma_1(\omega)$ is generally large below about 5000 cm^{-1} and much smaller above about 7000 cm^{-1}. For low x, on the other hand, the conductivity has roughly the same magnitude at 1000 and 10 000 cm^{-1}. This is in large part due to a transition at around 10 000 cm^{-1}, which is particularly strong in the low x mixed-valent region. As discussed in the next section, we associate this transition with excitations between the Fermi level and a nearby (localized) f level on the Yb. In the evolution from the mixed-valent region (low x) to the heavy-fermion regime (high x) this feature moves to higher frequency, reflecting an increased separation between the f level and Fermi level. Our infrared data also show considerable

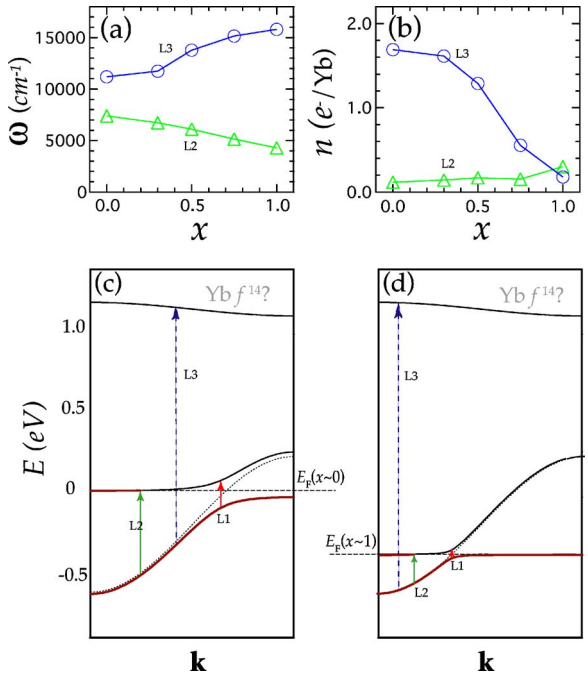

FIG. 13. (Color online) (a) The center frequencies of the transitions L2 and L3 from (Fig. 5), and (b) the strengths of the corresponding Lorentzian fit components are shown as a function of doping, x. A band structure picture which we use to interpret the trends in (a) and (b) is shown for (c) $YbInCu_4$ and (d) $YbAgCu_4$. The dashed lines illustrate **k**-conserving transitions which we associate with L1, L2, and L3, respectively. (L1 is the Kondo resonance excitation.)

weakening of this transition with increasing x. This may be associated with changes in hybridization and dipole matrix-element strength as one moves away from the mixed-valent regime. It is the strength of this transition in the mixed-valent regime that leads to the more or less constant slope of $n(\omega)$ for $x=0$ and 0.3.

Like the frequency dependence of $n(\omega)$, the temperature dependence also changes qualitatively as a function of x. For low x, the behavior of $n(\omega)$ in the low frequency region (below about 7000 cm^{-1}) is dominated by the growth of the Kondo resonance at low temperature. As a consequence, the low-temperature value of $n(\omega)$ exceeds the high-temperature value up to about 9000 cm^{-1} (where they cross) for low x. In contrast, for $x=1$, the high-temperature value exceeds the low-temperature value of $n(\omega)$. These observations reflect fundamental differences in the temperature dependence of $\sigma_1(\omega)$ in the high- and low-x regions, as shown in detail in Figs. 3 and 4.

V. DISCUSSION; HIGH FREQUENCY TRANSITIONS

We now consider the x-dependent trends in the high frequency ($\omega > 6000$ cm^{-1}) conductivity. We will use the language in Fig. 5 (Sec. I) associated with Lorentzian fitting of the conductivity data, focusing our attention on the features L2 and L3. In Figs. 13(a) and 13(b) we show the center frequency and strength of these high energy excitations as a

function of x. This measured x dependence can enhance our understanding of the nature of the underlying states associated with these transitions and the density of states near E_F.

In a textbook picture of metals and semiconductors, an important effect of doping is to add or remove electrons from a set of band states, thereby influencing the position of E_F. In $YbIn_{1-x}Ag_xCu_4$, increasing x from 0 to 1 corresponds to the net removal of two electrons (per formula unit) from the system, hence we expect the Fermi level to move downward in energy as x is increased. Relativistic band structure calculations addressing these changes have been carried out by Antonov *et al.*[26] In this scenario, optical features involving transitions from filled states just below E_F tend to weaken and move upward as x is increased and these states are emptied.[60] The dashed arrow of Fig. 13(c) illustrates one such transition, which we identify with L3. In this scenario, the width of the feature when $x=0$ suggests bandwidths of order ~ 1 eV, and the threshold for these transitions, approximately 7000 cm^{-1} (~ 0.9 eV) when $x=0$, gives an indication of the overall energy position relative to E_F. Furthermore, the amount of shift with doping implies that the density of states in the near-E_F region of the band structure is approximately $2/0.58\ \text{eV} \sim 3.5\ e^-\ \text{eV}^{-1}/\text{f.u.}$ Both of these numbers are quite reasonable for conduction bands in rare earth and transition metal systems.[55]

With this rigid band interpretation as a backdrop describing the salient relationships between L3 and x, the correlated electron effects discussed in previous sections occur in addition. The renormalization discussed there dresses these bare states and the renormalized region of the band structure, including the Kondo resonance, tracks E_F, which moves downward with increasing x.

We now turn to the systematics of the feature L2. Here we explore the possibility that this feature is associated with the upper cutoff in our model calculation [Fig. 8(a) and Eq. (4)], which is suggested by the coincidence between the energy of the L2 feature and that of the upper cutoff. Unlike L3, the strength of L2 is nearly independent of x, which directs our attention away from a simple band interpretation. When considering an identification of the component L2, we point out the significant temperature dependence in the frequency region associated with L2, as shown in Figs. 2, 3, and 11. The temperature dependent interplay of spectral weight contained in the frequency intervals of L1 and L2 leads one naturally to speculate that perhaps the same correlated electron physics controlling L1 may also be relevant to L2. One is thus led toward the question of whether the L2 feature represents a further phenomenon associated with hybridization physics.

We noted in Sec. II that in addition to the strong peak in the PAM conductivity associated with renormalized band nesting, a second feature could appear at higher frequencies associated with the initial state energy crossing E_F. In a linearly dispersing band model, this change occurs around the conduction electron bandwidth frequency [Eq. (4)]. In a more realistic bandstructure, the filling fraction and band curvature details could influence the frequency and magnitude of this conductivity change. In particular, if the transition final states are band edge states, then significant shifting with doping concentration could result.

With these considerations, it is reasonable to suggest that L2 represents a conductivity feature arising from Fermi surface quasiparticles. The narrowness can then be attributed to the very long lifetime of the initial state (because it occurs on the Fermi surface), and weak x dependence of the strength arises because the energy structures responsible for the associated transitions track the x-dependent Fermi level, as opposed to becoming filled or depleted with x. The culmination of the identifications suggested in this section are presented at a light and heavy doping concentration in Figs. 13(c) and 13(d), respectively.

VI. DISCUSSION, THE PHASE TRANSITION OF $YbInCu_4$

The physical mechanism of the phase transition in the lightly doped system remains elusive, however, progress has been made in understanding aspects of the phase transition. In previous sections, we have analyzed in detail the low temperature, conductivity in terms of PAM renormalizations of few-band models. We now discuss how this picture identifying optical transitions may be related to the interesting phenomenology displayed by $YbIn_{1-x}Ag_xCu_4$ including the phase transition at low x.

The Kondo volume collapse[12] (KVC) model, which describes the complex interplay of the system volume, hybridization, Kondo temperature, and f level occupation, seems adequate to describe the valence transition in elemental Ce.[12,56] This model, however, seems insufficient to quantitatively describe the phase transition in $YbInCu_4$, as evidenced mainly by the smallness of the volume change at the transition. Some authors[3,17,38] have argued that a quasigap, or region of low density of states, exists in the bare band structure located just above the Fermi level in $YbInCu_4$, and is important to the phase transition. This description is qualitative, but addresses the change in carrier density as well as the changes related to Kondo physics. In this approach, the presence of a quasigap makes the Kondo temperature very sensitive to the placement of the Fermi level and can help induce the phase transition in manner akin to the KVC model, but with the importance placed on the density of states dependence, rather than the volume.

It is of interest to ask what consequences a quasigap scenario could have for the optical data in $YbInCu_4$, where the conductivity in the range of 8000 cm^{-1} (L2 in the fits) drastically displaces to lower frequency forming the Kondo resonance excitation (L1) discussed above. In the picture outlined in Fig. 13(c), an upward shift in the Fermi level off of the bare band edge and into the quasigap could have drastic consequences for the optical response, possibly forcing the contribution L2 to shift to very high frequency, as the renormalized portion of the upper band is forced across the gap in response to a small shift in E_F. This possible interpretation of the temperature dependence indicates that further theoretical work directed toward investigating the generic physics of the PAM and the fate of the Kondo scenario in the context of rapidly varying band structure is needed to understand the complex temperature dependence of $YbInCu_4$.

Theoretical work on the Falicov-Kimball model[33–35] attempts to make a quantitative connection with experiment using a particular many-body model which features a first order phase transition. Aspects of this modeling seem prom-

ising, in particular the prediction of substantial temperature dependence of the high frequency optical conductivity, however, this model does not yet explicitly include the effects of hybridization. It is possible that a minimal model that describes the first order phase transition and also includes the Kondo physics may require and extension of the periodic Anderson model to include Falicov-Kimball-type interaction.

VII. CONCLUSIONS

Our results indicate that T_K scaling is present in the low temperature finite-frequency dynamics of $YbIn_{1-x}Ag_xCu_4$ and can be addressed in the context of local-moment models. Furthermore, our data provide numerical estimates of key parameters necessary for the construction of a minimal theoretical model of the valence transition as well as pointing out salient features of the underlying band structure. Further work may be directed toward greater understanding of this low-T scaling behavior as well as unexplained temperature-dependent behavior of lightly doped $YbIn_{1-x}Ag_xCu_4$.

ACKNOWLEDGMENTS

The authors have greatly benefited from discussions with D. N. Basov, K. S. Burch, A. L. Cornelius, D. L. Cox, P. A. Lee, B. S. Shastry, and A. P. Young. We also gratefully acknowledge S. L. Hoobler and Y. W. Rodriguez for technical assistance. Work at UCSC was supported by NSF Grant No. DMR-0071949. Z.F. acknowledges the support of NSF Grant No. DMR-0433560.

*Present address: Stanford University, Geballe Laboratory for Advanced Materials and Stanford Synchrotron Radiation Laboratory, Stanford University, Stanford, California 94305, USA.
†Electronic address: jhancock@stanford.edu

[1] J. M. Lawrence, G. H. Kwei, J. L. Sarrao, Z. Fisk, D. Mandrus, and J. D. Thompson, Phys. Rev. B **54**, 6011 (1996).
[2] J. L. Sarrao, C. D. Immer, C. L. Benton, Z. Fisk, J. M. Lawrence, D. Mandrus, and J. D. Thompson, Phys. Rev. B **54**, 12207 (1996).
[3] A. L. Cornelius, J. M. Lawrence, J. L. Sarrao, Z. Fisk, M. F. Hundley, G. H. Kwei, J. D. Thompson, C. H. Booth, and F. Bridges, Phys. Rev. B **56**, 7993 (1997).
[4] C. D. Immer, J. L. Sarrao, Z. Fisk, A. Lacerda, C. Mielke, and J. D. Thompson, Phys. Rev. B **56**, R71 (1997).
[5] J. M. Lawrence, S. M. Shapiro, J. L. Sarrao, and Z. Fisk, Phys. Rev. B **55**, 14467 (1997).
[6] B. Kindler, D. Finsterbusch, R. Graf, F. Ritter, W. Assmus, and B. Luthi, Phys. Rev. B **50**, 704 (1994).
[7] J. De Teresa, Z. Arnold, A. del Moral, M. Ibarra, J. Kamarad, D. Adroja, and B. Rainford, Solid State Commun. **99**, 911 (1996).
[8] I. Felner and I. Nowik, Phys. Rev. B **33**, 617 (1986).
[9] I. Felner *et al.*, Phys. Rev. B **35**, 6956 (1987).
[10] J. Sarrao, C. Immer, Z. Fisk, C. Booth, E. Figueroa, J. Lawrence, A. Modler, A. Cornelius, M. Hundley, G. H. Kwei *et al.*, Phys. Rev. B **59**, 6855 (1999).
[11] J. W. van der Eb, Ph.D. thesis, University of Groningen, 2000.
[12] J. W. Allen and R. M. Martin, Phys. Rev. Lett. **49**, 1106 (1982).
[13] A. Mitsuda, T. Goto, K. Yoshimura, W. Zhang, N. Sato, K. Kosuge, and H. Wada, Phys. Rev. Lett. **88**, 137204 (2002).
[14] T. Park, V. A. Sidorov, J. L. Sarrao, and J. D. Thompson, Phys. Rev. Lett. **96**, 046405 (2004).
[15] T. Mito, T. Koyama, M. Shimoide, S. Wada, T. Muramatsu, T. C. Kobayashi, and J. L. Sarrao, Phys. Rev. B **67**, 224409(R) (2003).
[16] I. Svechkarev, A. Panfilov, S. Dolja, H. Nakamura, and M. Shiga, J. Phys.: Condens. Matter **11**, 4381 (1999).
[17] J. L. Sarrao, A. P. Ramirez, T. W. Darling, F. Freibert, A. Migliori, C. D. Immer, Z. Fisk, and Y. Uwatoko, Phys. Rev. B **58**, 409 (1998).
[18] R. Hauser, L. Naber, G. Schaudy, E. Bauer, G. Hilscher, B. Kindler, and W. Assmus, Czech. J. Phys. **46**, 2543 (1996).
[19] C. Dallera, M. Grioni, A. Shukla, G. Vanko, J. L. Sarrao, J. P. Rueff, and D. L. Cox, Phys. Rev. Lett. **88**, 196403 (2002).
[20] J. J. Joyce, A. B. Andrews, A. J. Arko, R. J. Bartlett, R. I. R. Blythe, C. G. Olson, P. J. Benning, P. C. Canfield, and D. M. Poirier, Phys. Rev. B **54**, 17515 (1996).
[21] P. Weibel, M. Grioni, D. Malterre, B. Dardel, Y. Baer, and M. Besnus, Z. Phys. B: Condens. Matter **91**, 337 (1993).
[22] J. M. Lawrence, G. H. Kwei, P. C. Canfield, J. G. DeWitt, and A. C. Lawson, Phys. Rev. B **49**, 1627 (1994).
[23] F. Reinert, R. Claessen, G. Nicolay, D. Ehm, S. Hufner, W. P. Ellis, G. H. Gweon, J. W. Allen, B. Kindler, and W. Assmus, Phys. Rev. B **58**, 12808 (1998).
[24] S. R. Garner, J. N. Hancock, Y. W. Rodriguez, Z. Schlesinger, B. Bucher, Z. Fisk, and J. L. Sarrao, Phys. Rev. B **62**, R4778 (2000).
[25] J. N. Hancock, T. McKnew, Z. Schlesinger, J. L. Sarrao, and Z. Fisk, Phys. Rev. Lett. **92**, 186405 (2004).
[26] V. N. Antonov, M. Galli, F. Marabelli, A. N. Yaresko, A. Y. Perlov, and E. Bauer, Phys. Rev. B **62**, 1742 (2000).
[27] F. Marabelli and E. Bauer, J. Appl. Phys. **73**, 5418 (1993).
[28] J. Sarrao, Physica B **259-261**, 128 (1999).
[29] M. Dzero, L. Gor'kov, Z. Fisk, and A. Zvezdin, Physica B **312-313**, 321 (2002).
[30] N. Mushnikov, T. Goto, K. Yoshimura, and W. Zhang, Physica B **334**, 54 (2003).
[31] A. Schroder, G. Aeppli, R. Coldea, M. Adams, O. Stockert, H. v. Lohneysen, E. Bucher, R. Ramazashvili, and P. Coleman, Nature (London) **407**, 351 (2000).
[32] T. Giamarchi, C. M. Varma, A. E. Ruckenstein, and P. Nozieres, Phys. Rev. Lett. **70**, 3967 (1993).
[33] V. Zlatic and J. K. Freericks, Acta Phys. Pol. B **32**, 3253 (2001).
[34] J. K. Freericks and V. Zlatic, Phys. Status Solidi B **236**, 256 (2003).
[35] J. K. Freericks and V. Zlatic, Rev. Mod. Phys. **75**, 1333 (2003).
[36] M. Dressel and G. Gruner, *Electrodynamics of Solids: Optical Properties of Electrons in Matter* (Cambridge University Press, Cambridge, 2002).
[37] A. Wooten, *Optical Properties of Solids* (Academic Press, New York, 1972).

[38] E. Figueroa, J. Lawrence, J. Sarrao, Z. Fisk, M. Hundley, and J. Thompson, Solid State Commun. **106**, 347 (1998).
[39] A. N. Tahvildar-Zadeh, M. Jarrell, T. Pruschke, and J. K. Freericks, Phys. Rev. B **60**, 10782 (1999).
[40] V. T. Rajan, Phys. Rev. Lett. **51**, 308 (1983).
[41] A. Hewson, *The Kondo Problem to Heavy Fermions* (Cambridge University Press, Cambridge, 1993).
[42] M. Jarrell, Phys. Rev. B **51**, 7429 (1995).
[43] N. Vidhyadhiraja, V. Smith, D. Logan, and H. Krishnamurthy, J. Phys.: Condens. Matter **15**, 4045 (2003).
[44] A. Georges, G. Kotliar, W. Krauth, and M. Rozenberg, Rev. Mod. Phys. **68**, 13 (1996).
[45] D. Edwards, in *Narrow Band Phenomena*, NATO Advanced Institute Series (Plenum, New York, 1988).
[46] A. J. Millis and P. A. Lee, Phys. Rev. B **35**, 3394 (1987).
[47] D. L. Cox, C. Tannous, and J. W. Wilkins, Phys. Rev. B **33**, 2132 (1986).
[48] L. Degiorgi, Rev. Mod. Phys. **71**, 687 (1999).
[49] P. Coleman, Phys. Rev. Lett. **59**, 1026 (1987).
[50] D. L. Cox (private communication).
[51] A. J. Millis, M. Lavagna, and P. A. Lee, Phys. Rev. B **36**, R864 (1987).
[52] N. Grewe, Z. Phys. B: Condens. Matter **56**, 111 (1984).
[53] J. Demsar, R. D. Averitt, K. H. Ahn, M. J. Graf, S. A. Trugman, V. V. Kabanov, J. L. Sarrao, and A. J. Taylor, Phys. Rev. Lett. **91**, 027401 (2003).
[54] G. D. Mahan, *Many-Particle Physics* (Plenum, New York, 1990).
[55] H. Ibach and H. Luth, *Solid State Physics: An Introduction to the Principles of Materials Science* (Springer, New York, 1995).
[56] K. Haule, V. Oudovenko, S. Y. Savrasov, and G. Kotliar, Phys. Rev. Lett. **94**, 036401 (2005).
[57] In the N-fold degenerate Anderson impurity model, the value of the low temperature susceptibility is related (Ref. 41) simply to the Kondo temperature T_K by $\chi(0)=(g\mu_B)^2 j(j+1)w_N/3k_BT_K$, where w_N is given by Eq. (11).
[58] Strictly speaking, there appears a peak in the density of states in the impurity case. The periodic system differs in that an additional *indirect* gap within this peak is present (Ref. 44).
[59] T_L here is a common alternative definition of the Kondo temperature (Refs. 3 and 40) and is related to the Kondo temperature T_K by Ref. 41 Eq. (10).
[60] Similarly, optical features involving final states just above E_F may strengthen as x is increased and additional final states become available.